Earth and Space Science

RESEARCH ARTICLE
10.1029/2019EA000935

Semiautomated Identification and Characterization of Dunes at Hargraves Crater, Mars

A. Emran[1,2], L. J. Marzen[2], and D. T. King Jr.[2]

[1]Center for Space and Planetary Sciences, University of Arkansas, Fayetteville, AR, USA, [2]Department of Geosciences, Auburn University, Auburn, AL, USA

Key Points:
- Individual barchan and barchanoidal dunes were extracted from a semiautomated object-based image analysis technique
- The dunes are labeled as active with a stability index of 2 and have not been influenced by subsurface water ice or volatile
- The validated and accurate result in this study indicates the applicability of the OBIA method for the entire surface of Mars

Supporting Information:
- Supporting Information S1

Correspondence to:
A. Emran,
alemran@uark.edu

Citation:
Emran, A., Marzen, L. J., & King, D. T., Jr. (2020). Semiautomated identification and characterization of dunes at Hargraves crater, Mars. *Earth and Space Science*, 7, e2019EA000935. https://doi.org/10.1029/2019EA000935

Received 6 OCT 2019
Accepted 1 AUG 2020
Accepted article online 7 AUG 2020

Abstract The Mars Global Digital Dune Database (MGD^3) contains information on Martian dune fields and prepared manually from the Thermal Emission Imaging System (THEMIS; 100 m/pixel) images. Although the MGD^3 outlines dune fields, it overlooks the recognition of smaller dune forms. This paper aims to identify individual dunes from a semiautomated object-based image analysis technique and characterize dune materials at Hargraves crater, Mars. MGD^3 would benefit to be updated for an improved understanding of the Martian surface and its atmospheric mechanisms at a local scale. An object-based image analysis technique was applied here to the Context Camera (CTX; 6 m/pixel) data set to extract dune data in a more efficient, reliable, and accurate fashion. This study is a test case in validating a remote sensing method that has wide applicability to the entire Martian surface resulting in an update to the dune database at a higher spatial resolution—providing a better understanding of surface and atmospheric behavior of Mars at the local scale. We also explored the wind flow and dune stability—presenting an insight into the dune modification mechanism—within the crater. The prevailing wind inside the crater flows to the west-northwest. The dunes are labeled as active (stability index of 2) and do not appear to have been influenced by subsurface water ice or volatiles. We emphasize that the technique used here has a wide prospect in temporal monitoring of dune sediment flux, dune migration or erosion rates, improving near-surface airflow modeling, and dune stability analysis.

Plain Language Summary The Mars Global Digital Dune Database (MGD^3) contains morphologic information on Martian dune fields. MGD^3 has various science applications including atmospheric circulation modeling, planetary climate change, mechanical weathering processes, and future rover lander missions to Mars. However, the database was prepared manually through visual photointerpretation from low-resolution satellite images of 100 m/pixel and, consequently, overlooked the recognition of smaller dune forms. Thus, MGD^3 would benefit to be updated for an improved understanding of the Martian surface and its atmospheric mechanisms including near-surface wind patterns at a local scale as opposed to the global scale. We used a semiautomated object-based image analysis (OBIA) technique from higher-resolution images of ~6 m/pixel—more than 10 times higher spatial resolution compared to the previous imagery. Using the technique, we extracted individual dunes at Hargraves crater in a more efficient, reliable, and accurate fashion. The validated and accurate result in this study indicates the applicability of the OBIA method for the entire surface of Mars. Thus, the application OBIA method will be a great improvement for futures studies on Martian (and terrestrial) dune fields including temporal monitoring with better estimates of sediment flux, dune migration or erosion rates, and improving near-surface airflow modeling.

1. Introduction

The surface of Mars is home to eolian dune fields in a variety of locations (e.g., Bandeira et al., 2010; Edgett & Christensen, 1991). Dune materials and eolian processes pave the way to understanding the interactions between the surface and atmosphere of the planet, as well as the weather, climate, and climatic evolution during Martian history (e.g., Greeley et al., 2001; Wilson & Zimbelman, 2004). On Earth, where field observations are possible, dune fields have been studied in conjunction with satellite remote sensing in order to understand their evolution of eolian sand dunes (e.g., Elbelrhiti et al., 2008; Hugenholtz et al., 2012). This integration of remote sensing and advanced quantitative investigation allows an understanding of the relationship between patterns of atmospheric circulation and transport of regional sediments (e.g., du Pont et al., 2014; Fenton et al., 2014). However, in the instance of Mars, direct field observation of dunes, wind

velocities, and atmospheric circulation trends are not available in quantity so far, even though the relationship between bedform and atmospheric circulation are of critical interest for the understanding of atmospheric dynamics (Vaz et al., 2015).

Over the past few decades, studies have been done to better understand Martian surface processes and global scale atmospheric dynamics from the analysis of various eolian processes and wind-related features (e.g., Fenton et al., 2005; Gardin et al., 2012; Hayward et al., 2009; Sefton-Nash et al., 2014; Silvestro et al., 2010; Ward et al., 1985). Regional-scale dunes (and dune fields) were first detected on Mars during the early 1970s in Mariner 9 images (Sagan et al., 1972). Later, more dunes were detected from high-resolution orbital images of Mars Global Surveyor (MGS) during the late 1990s (Edgett & Malin, 2000) and were found to have similarities with dunes of Earth (Bandeira et al., 2010). Recently, a comprehensive catalog for the Martian dune fields was created by a group of planetary scientists and is called the Mars Global Digital Dune Database (MGD^3) (Hayward et al., 2007, 2014). This compiled database has a nearly global view, encompassing a surface area from latitude 65°N to 65°S (the equatorial region), from 60°N to 90°N (the north polar region), and from 60°S to 90°S (the south polar region), facilitating understanding in relationships between the Martian global atmospheric circulation and sediment dynamics (Hayward et al., 2007, 2014).

The delineation of dune fields in MGD^3 was prepared manually through visual photointerpretation from the Thermal Emission Imaging System (THEMIS; Christensen et al., 2004) onboard the 2001 Mars Odyssey, which yielded specific imagery at 100 m/pixel spatial resolution (Hayward et al., 2007, 2014). The database contains information of regional to planetary scale dunes and dune fields (>1 km^2) including classification of dune morphologies, digitized dune parameters, that is, area, and mapped dune slipface orientations with the trends of the prevailing surface winds estimated from the measured dune slipface orientation and gross dune morphology (Gullikson et al., 2018; Vaz et al., 2015). Although the MGD^3 outlines dune fields, it does not delineate individual dunes within the dune fields. Moreover, manual digitization of the individual dune parameters (e.g., shape, size, area, and elevation) from the lower spatial resolution THEMIS images is a very arduous, labor-intensive, and time-consuming task. Thus, a semiautomated method from high spatial resolution images, for example, the Context Camera (CTX; Malin et al., 2007) or the High Resolution Imaging Science Experiment (HiRISE; McEwen et al., 2007), is more efficient at maximizing the extraction of significant surface morphological information about Martian dune fields (Bandeira et al., 2010; Vaz et al., 2015).

Many studies on Martian dune fields have been conducted over the past few decades (e.g., Bandeira et al., 2010; Emran et al., 2019; Vaz & Silvestro, 2014; Vaz et al., 2015), and of those studies, some used traditional manual digitization of dune parameters and other geomorphic characteristics using satellite images (e.g., Greeley & Thompson, 2003; Fenton, Michaels, & Beyer, 2014; Fenton, Michaels, Chojnacki, et al., 2014; Silvestro et al., 2010). Extracting dune parameters from orbital data sets is not only cumbersome but also involves some degree of user bias (Hugenholtz et al., 2012). That user bias yields difficulties in observational integration and standardization (Vaz et al., 2015). Recently, studies have applied automated detection of dune characteristics through the object-based image identifications (e.g., Bandeira et al., 2010, 2011; Sholes et al., 2013; Silvestro et al., 2013; Vaz & Silvestro, 2014; Vaz et al., 2015). The study of Vaz et al. (2015) used an object-based image classification for mapping and pattern characterization of dunes in Ganges Chasma and Gale crater, Mars, from CTX images. Sholes et al. (2013) developed a rule set in eCognition software for object-based classifications and demonstrated the validity of the method for use in planetary remote sensing. Vaz and Silvestro (2014) introduced a new set of object-based approaches for simple and quick mapping of dunes and characterization of local-scale eolian bedforms at the Mars Science Laboratory (MSL) landing site in Gale crater. Bandeira et al. (2011) used the Mars Orbiter Camera (MOC) data of the MGS probe through an automated method based on the extraction of local information from images for detection and delineation of dune fields on Mars. Most of these studies identified linear dune features (longitudinal and transverse dunes), which can be easily recognized through an automated method because of their identifiable linear slipface structure. In contrast, identification of small barchan and barchanoids are occasionally very difficult to detect from remote sensing image analysis techniques due to their obscured linear slipface (e.g., Vaz et al., 2015). Because of this higher level of difficulty to identify slipfaces of small barchan and barchanoidal dunes, the present study uses a semiautomated method for improved accuracy in the identification of nonlinear dunes at a local scale.

We used a semiautomated object-based image analysis (OBIA) approach for mapping and characterization of an intracrater dune field at Hargraves crater, Mars. The availability of extensive regional and local coverage compelled this study to choose CTX over the HiRISE data set. The CTX sensor has a spatial resolution of ~6 m/pixel, which provides a more comprehensive understanding of the Martian dune fields compared to the MGD[3] information constructed from THEMIS images. The delineation of the dune field in the MGD[3] for Hargraves is not accurate for the study area because the outline of the dune field does not cover all the dunes present (Figure 1). Moreover, the MGD[3] did not delineate individual dunes or their geometric information at the crater. The objective of identifying individual dunes at Hargraves is to correct the anomaly in the dune field delineation of MGD[3] as opposed to the manual pixel-based photointerpretation technique from the comparatively lower spatial resolution THEMIS data. A semiautomated method using CTX data and the generic algorithms of the OBIA technique was used for this analysis. This study tested the efficiency and accuracy of OBIA and its applicability to other Martian surfaces with the goal of making a higher-resolution dune database, ultimately updating the existing database. Our primary goal was to delineate individual dunes and their spatial information (e.g., outline, size, shape, area, and elevation) thereby improving the MGD[3]. Size, area, and elevation information are crucial for dune analysis since these parameters give a quantitative measure of the total amount of sediment present in a dune field or the amount of sediment transported to the dune field. Temporal data on area and elevation of a dune field provide an estimate of the amount of sediment added to or eroded from the dune field over time and can be investigated in future studies. Dune morphology along with information about the slipface and airflow within a dune field provides important clues about the surface-atmospheric behavior and the mechanism of dune modification. Therefore, after the delineation of individual dunes, we interpreted the wind pattern inside the crater by analyzing the raw slipface orientations of the dunes. Slipface information of the dunes was derived from the existing MGD[3] data set however, a future study can be conducted to identify and delineate the slipface features using an OBIA technique.

The study also determines the stability (modification) of the dunes inferred from the apparent presence or absence of specific features and morphological characteristics including the degree of influences of noneolian processes (e.g., mass wasting) to the surface morphology of dune field. These stability parameters were identified from higher-resolution CTX and HiRISE data. The stability analysis of the dune field indicates whether the dunes are active (mobile) or dormant. Though the stability of dunes can appropriately be analyzed using a time series change detection analysis (which is beyond the scope of the present study), we adopted a deterministic approach, same as the method of Fenton and Hayward (2010) and Gullikson et al. (2018), by analyzing the apparent morphologies of the dunes to infer their stability. A combination of wind movement and stability analysis provides an insight into the dune modification mechanism within the crater. We emphasize that the interpretation of wind movements and stability analysis of the dune field is not an improvement through the object-based method but rather to interpret the characteristics of the dunes inside the Hargraves crater using visual analysis of the available high-resolution data and existing data set. The objective of our study is to show how the application of OBIA can improve our understanding of the Martian surface and its atmospheric mechanisms including near-surface wind patterns at a local scale as opposed to the global scale. Application of this technique will be a great improvement for future dune field studies on the Martian surface including temporal monitoring with better estimates of sediment flux, dune migration or erosion rates, improving near-surface airflow modeling, and dune stability analysis.

2. Observations and Methods

2.1. Hargraves Crater

The Nili Fossae is a suite of concentric grabens in the northwest of the Isidis basin and north of Syrtis Major of Mars (Goudge et al., 2015). Approximately 50 km to the east of the Nili Fossae Trough (NFT) is the 65 km diameter Hargraves crater (Figure 1), which formed during the late Noachian or early Hesperian Period (Ivanov et al., 2012). The crater is a part of the Jezero crater watershed (Goudge et al., 2015) and its location is centered on 75.75°E, 20.75°N. The crater is home to a visible dune field at CTX resolution (Figure 1) and the MGD[3] records that the dune field has barchan (B) and barchanoid (Bd) dune types based on the dune classification method of McKee et al. (1979). McKee et al. (1979) define the barchan (B) as crescent in map view with a single slipface that indicates a wind movement toward one predominant direction. In

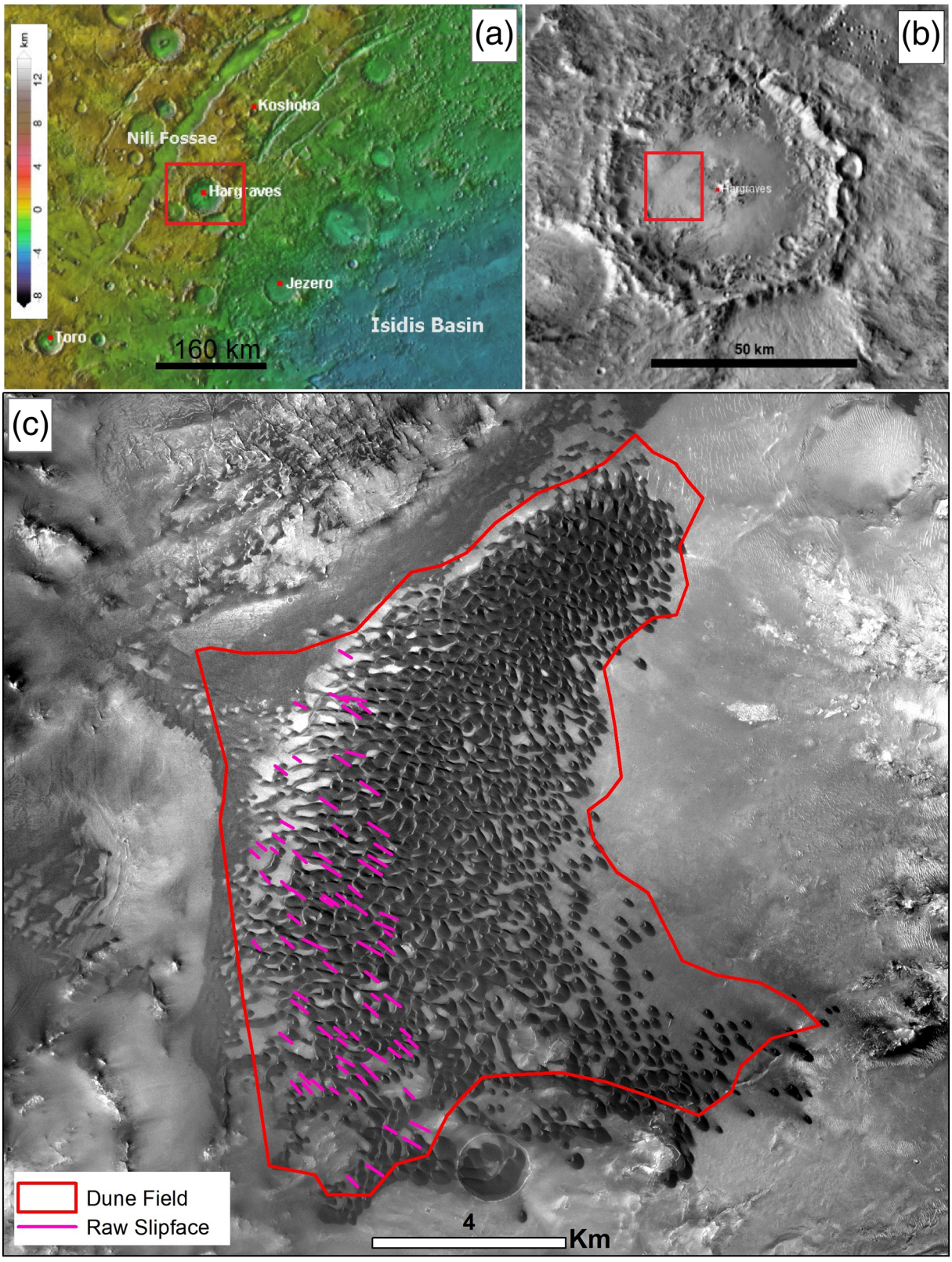

Figure 1. The location of the Hargraves crater is on the east side of the Nili Fossae Trough (NFT) and northwest of the Isidis Basin. (a) MOLA elevation data overlaid on THEMIS image mosaic. The red rectangle indicates the location in (b). (b) THEMIS daytime image of Hargraves crater. The red rectangle indicates the location in (c). (c) The dune field in CTX image resolution. The red outline is the dune field boundary and magenta transects are the raw slipface as defined by MGD[3]. North is up.

contrast, barchanoids (Bd) have a row of connected crescents in map view (merged together) with a single slipface (Hayward et al., 2007; McKee et al., 1979). The MGD[3] shows an absence of linear, star, and transverse dunes at Hargraves. Though the existing database did not find sand sheets in the study area, the visible CTX images show a thin sand apron present on the western part of the dune field. This study focuses on identifying individual barchans and barchanoidal dunes in the crater using higher-resolution images and the geological interpretation of the dunes from the dune field database parameters such as dune centroid, slipface, and wind vectors.

2.2. Data Set

We used images from the CTX and HiRISE sensors. Both instruments are onboard the National Aeronautics and Space Administration's (NASA's) Mars Reconnaissance Orbiter (MRO) spacecraft designed to study the atmosphere and geology of the planet.

2.2.1. CTX

The CTX instrument is a push-broom visible-image camera. CTX acquires monochromatic images at a spatial resolution of ~6 m/pixel and has a swath width of 30 km (Malin et al., 2007). Stereopair images are captured by CTX and can be used to produce high-resolution digital elevation models (DEMs) for topographic and morphologic mapping of the Martian surface. CTX stereopairs D14_032860_2009 and D15_033071_2009 were used as input layers in this study. Calibration, projection, and production of the DEM from CTX stereopairs were accomplished using the U.S. Geological Survey (USGS)'s Integrated Software for Imagers and Spectrometers (ISIS3) pipelines and NASA Ames Stereo Pipeline (ASP) stereogrammetry software (Beyer et al., 2014; Broxton & Edwards, 2008; Moratto et al., 2010). The CTX derived point cloud DEM was tied to the Precision Experiment Data Record (PEDR) point shot data of the Mars Orbiter Laser Altimeter (MOLA) instrument (Smith et al., 2001) using the *pc_align* function (Beyer et al., 2014) to account for the error of regional-scale topography (Goudge et al., 2017). The final DEM was coregistered with other data sets such as panchromatic image and rendered in eCognition and ArcGIS software for further analyses.

2.2.2. HiRISE

The HiRISE is a push-broom visible and near-infrared imager used for detailed analysis of surfaces at a nominal spatial resolution of ~25 cm/pixel (Delamere et al., 2010; McEwen et al., 2007). A detailed instrumental specification of the HiRISE sensor can be found in McEwen et al. (2007). The Martian surface composition and albedo heterogeneities are derived from HiRISE color images which are directly correlated to the results obtained from other orbital images, for example, CTX and THEMIS (Quantin-Nataf et al., 2018; Zurek & Smrekar, 2007). In this study, HiRISE images were used as a supplementary data set coupled with CTX images to interpret the fine-scale textural variation and used as a visual survey tool for local variability of the dune field. A list of HiRISE images used in this study is given in the appendix section. HiRISE data were used to visually identify the noneolian features (such as the presence of small pits or mass wasting features) in analyzing dune stability (modification) of the dune field.

2.3. OBIA

Traditional pixel-based image classifications have been widely applied in remote sensing image classification and feature extraction since the earlier era of satellite remote sensing. Pixel-based classification such as the maximum likelihood method, where each pixel is assigned to the highest probability class, has been regarded as a well-accepted paradigm in many remote sensing environmental applications (Castilla & Hay, 2008; Strahler et al., 1986). However, this technique has many limitations such as difficulties in processing high-resolution images due to “salt-and-pepper” effects (e.g., noise) and inability to distinguish child objects from their parents (e.g., shadow effects). Therefore, pixel-based remote sensing analysis sometimes yields unreliable findings (e.g., Blaschke et al., 2014; Sholes et al., 2013), and thus, pixel-based image classification has garnered some criticism during the past 20 years (Blaschke & Strobl, 2002; Burnett & Blaschke, 2003; Fisher, 1997). Due to the limitations of pixel-based methods for high-resolution image analysis, a new paradigm of OBIA, also known as geographic object-based image analysis (GeOBIA), has gained considerable attention among remote sensing applications (e.g., Baatz et al., 2008; Blaschke, 2010; Blaschke et al., 2014; Castilla & Hay, 2008; Hay & Castilla, 2008; Tzotsos & Argialas, 2008). Studies utilizing on object-based image classification illustrate its success in accounting for homogeneity, shape, texture, position, and other conditions of a complex image scene from high-resolution data (e.g., Sholes et al., 2013).

This study, therefore, employs a set of semiautomated object-based rule sets for identifying the individual dunes at Hargraves crater, Mars to take advantage of object-based image classification techniques.

2.3.1. Semiautomated Object-Based Dune Identification

The semiautomated object-based dune identification methodology consists of an application of image segmentation into a set of image objects whose parameters were then used to distinguish dunes from the nondune object using a commercial eCognition software package from Trimble Geospatial. OBIA image segmentation produces nonoverlapping homogeneous regions (image objects) from a complex image scene such as an image at the pixel level (e.g., Duro et al., 2012). For this study, the map projected CTX panchromatic image of D15_033071_2009 and the DEM (derived from CTX stereopair) were used as the input layers. The ancillary data layers, for example, slope, roughness index, and shaded relief, were produced from the DEM using ESRI's ArcMap GIS software's *Spatial Analyst Tools* and were integrated into the process tree for better segmentation and subsequent outputs. We used multiresolution segmentation (MRS) algorithm (e.g., Baatz & Schäpe, 2000) because it employs user-dependent parameters to attain a better image segmentation result. Thus, MRS has proven the most successful method (e.g., Witharana & Civco, 2014). MRS uses a bottom-up region-merging algorithm, which considers each pixel of the scene as an individual object (Darwish et al., 2003; Duro et al., 2012; Tian & Chen, 2007). The merging decisions of neighboring objects are undertaken considering local homogeneity based on user-defined parameters (e.g., Hay et al., 2003; Marpu et al., 2010). Thus, the values of the parameters used in the segmentation of one set of images by a particular user may not necessarily be applicable to other images used by a different user. That is, a global application of this technique may require different sets of segmentation parameters for different regions and different images. Therefore, we emphasize that the technique can be applied at a global scale by different teams to update the existing database.

Three parameters (scale, shape, and compactness) are used to control the MRS algorithm (e.g., Liu et al., 2012). The scale parameter is the most influential parameter that affects image classification by determining the size and amount of spectral variation within resultant image objects (e.g., Kim et al., 2011; Smith, 2010). The greater the scale parameter, the greater the likelihood of more pixels merging to larger objects. The shape parameter optimizes between spectral (color) and spatial (shape) homogeneity and determines the degree of smoothness, whereas the compactness parameter is used as a weighting factor to determine the closeness of pixels clustered in a segment of the resultant image objects (e.g., Baatz & Schäpe, 2000; Witharana & Civco, 2014). MRS algorithm creates image objects in an iterative procedure, whereby individual pixels are merged into a larger size segment until it reaches an upper object variance threshold (e.g., Witharana & Civco, 2014). The object variance threshold defines a homogeneity within image objects based on the weighting of user-defined parameters so that the fractal borders of the objects are minimized. For the mathematical formulation of multiresolution segmentation see Benz et al. (2004), Tian and Chen (2007), and Tong et al. (2012). Adjusting for optimal segmentation parameter values is done on an iterative trial-and-error basis and are subjected to visual inspection of the homogeneity output of image segmentation (e.g., Hay et al., 2003; Myint et al., 2011). Therefore, using the different combinations of homogeneity parameters (e.g., scale, shape, and compactness) with an iterative trial-and-error routine, a user creates a hierarchical network of image objects (Darwish et al., 2003).

In this study, we weighted the DEM and panchromatic layers during MRS as 1:4, respectively. Weighting value of image layers represents the relative influence of the layers in merging the pixels into image objects during the segmentation process. The CTX panchromatic data layer was given more weight than the DEM data layer in the segmentation algorithm since dune features are more visible in the panchromatic layer. We optimized our algorithm parameters (scale, shape, and compactness) until the resultant image objects represented individual dunes. In other words, image segmentation is complete when each of the image objects visually corresponds to the meaningful real-world objects of interest (e.g., Jones et al., 2019), in this case, individual dunes. Following image segmentation, the scale parameter was set to 40, shape was fixed to 0.6, and compactness was set to 0.5 (all parameter values are unitless). Any changes in the values of the parameters of this combination did not accurately merge pixels into image objects and, thus, failed to appropriately represent the dunes at Hargraves crater. A scale parameter value of 40 is sufficiently small enough to delineate the fine-scale individual dunes (Figure 2b). Since the scale parameter controls the size and has a direct effect on the accuracy of the resultant image objects (Kim et al., 2008; Myint et al., 2011; Smith, 2010), a comparative sensitivity of finer and coarser image segmentation scales (keeping others

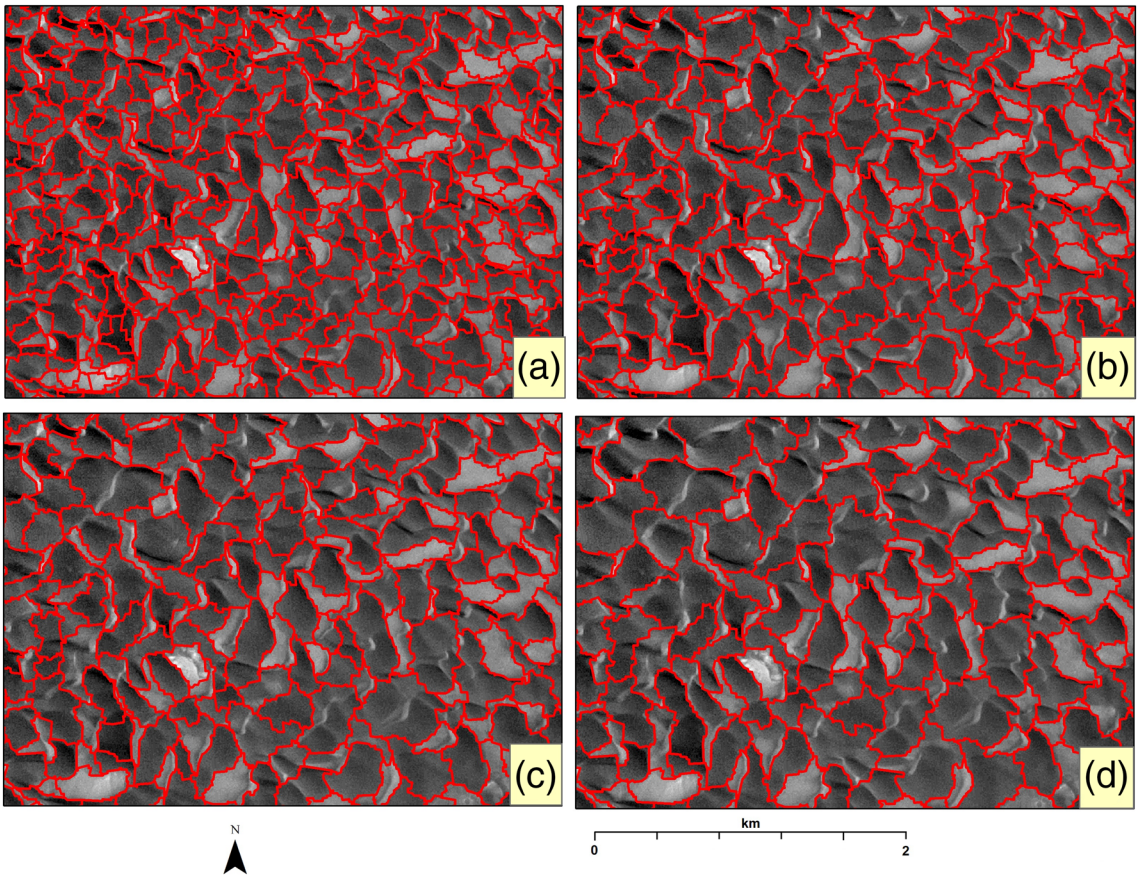

Figure 2. Semiautomated dune identification; a subset of image segmentation using a multiresolution segmentation algorithm. The individual red polygons are the distinct image objects result from a combination of parameters set based on iterative trial-and-error routine. The subset output of image objects from multiresolution segmentation of different MRS scale values: (a) MRS scale 30 (finer); (b) MRS scale 40 (considered optimum; used in this study); (c) MRS scale 50 (coarser); and (d) MRS scale 65 (coarser). Note that in all these different MRS scales, the other parameters were constant, that is, MRS shape to 0.6 and compactness to 0.5. For a detailed explanation of the sensitivity of these parameter combinations, readers are referred to the text section.

parameters as constant) applied to the study area (Figures 2a–2d) similar to previous OBIA studies (e.g., Duro et al., 2012; Myint et al., 2011). In the case of the finer segmentation scale parameter (e.g., MRS scale 30), the resultant image objects were too overcrowded and individual dunes consisted of multiple image segments (Figure 2a). Although a finer scale parameter (MRS scale <40) may produce image segments that represent individual dunes, the goal in segmentation is to use a sufficiently small enough scale so that each fine-scale individual dune is appropriately delineated. In contrast, the coarser segmentation scale (e.g., MRS scale 50 or 65) resulted in some image objects larger than individual dunes (Figures 2c and 2d). That is, for the larger-scale values (MRS scale >40) some of the individual image objects represent multiple dunes and, therefore, are not considered an optimum scale for this study.

After determining the appropriate scale parameter, we assessed the sensitivity of different combinations of shape and compactness parameters (keeping MRS scale of 40) in a fine-scale subset of the dunes (Figures 3a–3e). Figure 3a is a subset output derived from the combination of segmentation parameters used in this study, which shows an appropriate delineation of the individual dunes. In contrast, the other combinations of parameters failed to appropriately delineate individual dunes, despite having the same MRS scale of 40 in all combinations (Figures 3b–3e). Upon segmentation of image objects, a set of rules (e.g., object thresholding) were applied to the image objects to differentiate dunes from nondune objects. Object thresholding can separate the dune features from the nondune image objects by using a mean value at the image object level (in layer properties of image object) of the CTX grayscale image (e.g., mean raw digital number) and DEM (e.g., mean elevation values). In addition to using the panchromatic and DEM layers, slope, roughness index, and shaded relief layers were also examined to distinguish dune objects from nondune objects.

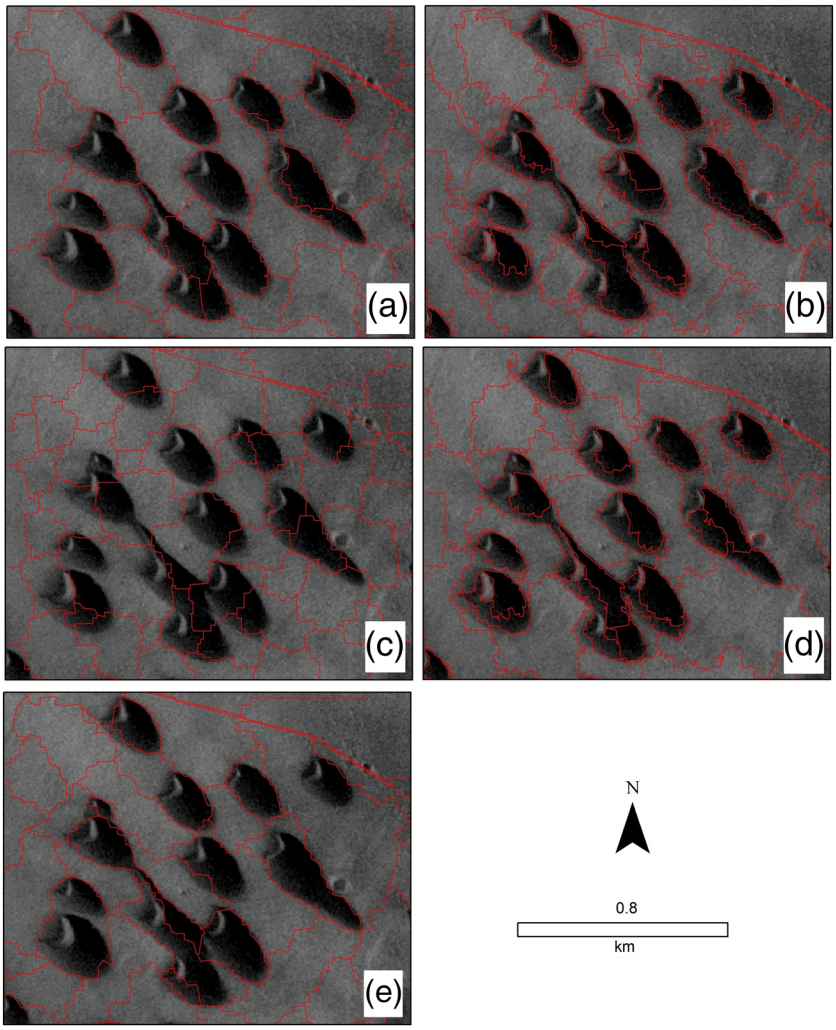

Figure 3. Comparison of image segmentation level tested in the object-based classification scheme. The subset output of image objects from multiresolution segmentation of different combinations of MRS shape and compactness parameters: (a) MRS shape 0.6 and scale 0.5 (used in this study); (b) MRS shape 0.1 and scale 0.1; (c) MRS shape 0.9 and scale 0.9; (d) MRS shape 0.1 and scale 0.9; and (e) MRS shape 0.9 and scale 0.1. Note that in all these different combinations of MRS shape and compactness parameters, the scale parameter was constant, that is, MRS scale of 40. (a) Is the combination used in this study. The other combinations failed to delineate the individual dunes appropriately, although having the same MRS scale in all combinations.

To calculate surface slope, the ArcGIS tool fitted a plane to the elevation values of neighboring 3×3 pixels around a center pixel (for details please see Burrough et al., 2015). Roughness index, derived from a DEM, represents the changes in elevation values between adjacent cells (Riley et al., 1999). These derived layers were not fed into the segmentation algorithms but used to manually help in algorithmically determining the detection of dunes. Any misclassified dune was assigned to the correct dune class from manual observations of the derived layers.

Unlike the use of multispectral and/or multispatial band images in most OBIA applications, this study only uses grayscale, single-band CTX images and the derived DEM for the object-based analysis. Thus, automated rule sets could not entirely distinguish all individual dunes in the study area. The identified dune objects were subsequently visually examined and then slightly modified in a way that a few unclassified dunes were merged to the automatically extracted dune objects and some misclassified nondune objects were excluded from the final classified dunes. After the dunes were extracted and classified, the spatially separated individual barchan and/or connected (barchanoidal) dunes were exported as individual polygon features. At this stage, the connected dunes were considered as separate features. The features were later exported (each

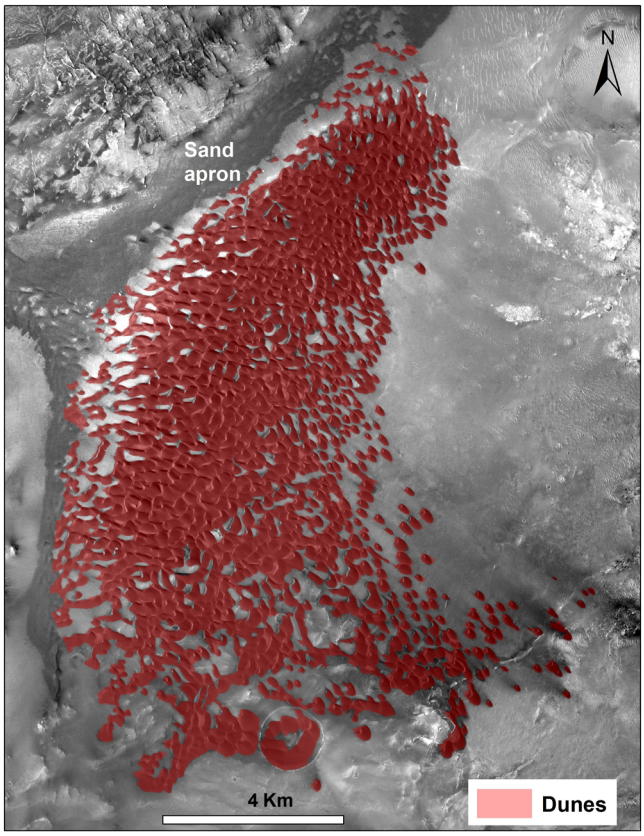

Figure 4. The final delineated dunes at Hargraves crater. The prepared dune vector (ESRI.shp) file overlain on CTX images. The red polygon indicates dunes. The thin sand aprons are shown in this figure. Note that the thin sand apron was not considered in the classification scheme in this study.

dune as an individual feature) from the classification scheme as a vector layer file. Each vector layer represents the individual dunes including all the geospatial information (e.g., coordinate, shape, geometry, length, and area). Lastly, the connected dunes were merged into individual barchanoidal dunes and the vector files were then ready for analysis in ESRI's ArcGIS software and merged into a single dune field vector layer, that is, shapefile. Similar to the existing database, only barchans and barchanoidal dune types were identified as defined by MGD[3] and the thin sand apron (see Figure 4) was not considered in the classification scheme in this study.

2.3.2. Accuracy Assessment

We assessed the accuracy of the OBIA-derived dune classification (i.e., quantitative validation) using a statistical test. The projected CTX images were used as the reference data set to evaluate the accuracy of the classified dunes. Exactly 500 random points were considered within the dune field outline using ArcGIS's *create random points* tool. Each of the points was carefully examined with the reference projected CTX image as to whether the dunes were identified accurately or not. An error matrix was used to evaluate the accuracy of the classification through assessing overall accuracy (OA) and kappa coefficient (kappa) statistics (e.g., Congalton, 1991; Congalton & Green, 2008; Foody, 2002). An error matrix (also known as confusion matrix) is a *nxn* array; where *n* refers to the number of classes used in accuracy assessment. In this case, *n* equals 2: dune and nondune classes. The error matrix calculates a producer and user accuracy of the classification based on the comparison, on a class-by-class basis, between reference points (the points that are known to be correct or ground truth point) and corresponding result from the classified or mapped points (generated from object-based analysis). A producer accuracy corresponds to the error of omission or exclusion in the classification. In other words, how many mapped points accurately represent the corresponding reference class points. In this study, the producer accuracy was calculated by dividing the number of accurately classified points in each group (dune and nondune) by the number of the reference points known to be of the corresponding group. In contrast, user accuracy indicates the error of commission or inclusion in the classification—how many mapped points truly represent the accurate class among the total mapped points of the corresponding class. We computed user accuracy by dividing the number of correctly classified points in each group (dune and nondune) by the total number of points that were classified in the respective group.

The study calculated the overall accuracy (OA) and kappa coefficient (kappa) statistics based on the result of the error matrix. Overall accuracy indicates what proportion of data were classified correctly and expressed as a percent. An overall accuracy of 100% means a perfect classification where all mapped points are classified accurately to the reference points. Overall accuracy was computed by dividing the total number of correctly classified points (sum of the correctly identified points in the dune and nondune classes) by the total reference points. Conversely, kappa statistics quantitatively evaluates how well the classification performed as compared to just randomly assigning values. Kappa values range from −1 to 1 with 0 indicates the classification is no better than a random classification. Kappa value is calculated as (Viera & Garrett, 2005)

$$k = \frac{Po - Pe}{1 - Pe}, \tag{1}$$

where *Po* refers to the observed agreement and P_e indicates expected agreement. *Po* can be calculated as (Viera & Garrett, 2005)

$$P_o = (P_{11} + P_{22})/P, \tag{2}$$

Table 1
The Reference Table on the Types and Characteristics of Morphological Dune Field Classes (Fenton & Hayward, 2010) and Their Respective Stability Index Used to Characterize the Dunes at Hargraves Crater

Stability index	Characteristics of morphological feature
1	Identifiable dunes, crisp slipface brinks
2	Partial apron, slipface brinks may be rounded
3	Aprons span interdunes, slipface brinks often rounded
4	Aprons often span interdunes, slipface brinks often rounded, somewhat dissected surface
5	Slipfaces difficult to identify, dissected appearance
6	No dunes present

Note. The table was recreated after Banks et al. (2018).

where P_{11} and P_{22} indicate the total number of points that are accurately classified to the dune and nondune classes (ground truth), respectively (see Table 4 for the symbol values). P indicates the total number reference points. Conversely, Pe can be expressed as (Viera & Garrett, 2005)

$$P_e = [(P_{01}/P)*(P_{10}/P) + (P_{02}/P)*(P_{20}/P)]. \quad (3)$$

The values of the P_{01}, P_{10}, P_{02}, and P_{20} are found from the error matrix table (see Table 3). The results of the accuracy assessment are described in section 3.

2.4. Dune Modification and Stability

We also analyzed the dune modification and stability of dune materials at Hargraves crater using the available higher-resolution images. Fenton and Hayward (2010) mapped and categorized the Martian dune fields into six morphological classes (see Table 1). The dune classes vary in apparent levels of eolian activity in the dune field and represent whether dunes are potentiality active or inactive and susceptible to erosion. Their classification scheme was based on an inferred dune stability scale constructed upon the apparent presence or lack of superposed noneolian features (such as gullies, small pits, and mass wasting features) as well as the apparent level of degradation (or modification) by noneolian processes (Banks et al., 2018). A stability index (SI) value (1 through 6, where a higher number indicates increasing evidence of stability or higher level of modification) was assigned to the dune classes. The six dune classes and their respective stability index and characteristics are given in Table 1.

Determining an appropriate stability index value is a subjective procedure based on the presence or absence of specific features such as identifiable dunes, crisp slipface, and presence of sand aprons (Fenton & Hayward, 2010). For detail of the dune stability derivation at the Martian global dune fields, the readers are referred to the relevant literature (e.g., Banks et al., 2018; Fenton & Hayward, 2010; Gullikson et al., 2018). However, the existing literature focuses on the stability index of regional-scale dune fields on Mars. For example, the recent study of Gullikson et al. (2018) attempted to expand dune field stability index to the existing MGD[3]. However, their work was confined to dune fields of 300 km^2 or larger in the equatorial and south polar regions. We apply the same methodology of Fenton and Hayward (2010) to characterize the dune stability in the crater on a significantly local scale.

High-resolution CTX and HiRISE data sets were used to identify evidence of eolian activity or erosion and the apparent dune morphology in the Hargraves crater dune field in determining appropriate SI of the dune materials. The presence of features like gullies, small pits, and mass wasting features are interpreted as the indication of recent noneolian activities (Gullikson et al., 2018). The stability index was determined based on the prevalence and magnitude morphological features such as rounded dune brinks, presence of a sharp-edged sand apron around the dune field, and a dissected surface. For instance, the absence of rounded dune brinks and sharp-edged apron are consistent with eolian inactivity or paucity of sand transport allowing the influence of other erosional or depositional processes to dominate dune morphology (Gullikson et al., 2018). The information on prevailing wind flow and dune stability index provides an insight into an improved understanding of the dune modification mechanism within the crater and can eventually be added to the existing data set.

3. Results and Discussions

3.1. Dune Identification

A vector (ESRI.shp) file was produced for the dunes, that is, barchans and barchanoids at the study area. The MGD[3] indicates that the dune field of Hargraves is a single dune field entity (though it does not correctly delineate appropriate dune field outline as given in Figure 1), but the dune database prepared in this project includes individual dunes and their geometric information (length, perimeter, and area). The method of dune identification is validated both qualitatively through visual interpretation and quantitatively through descriptive statistics. Average elevation was calculated for the dunes at Hargraves as −1,870 m with reference to the Mars datum whereas the MGD[3] defined elevation for the entire dune field as −1,851 m. One

Table 2
Details of the Statistical Analysis of MGD[3] Polygon Comparing With Our Output Objects-Based Polygon

Description of items	Areal difference (in km^2) [a]	Percent of areal over (+) or under (−) estimation[a]
Gross overestimation of dune field	30	+40%
Unmapped dunes by MGD[3]	7	−10%
Nondune overestimation by MGD[3]	37	+55%

Note. The unmapped dune (barchan and barchanoids) and overestimated nondune areas by MGD[3] and their percentages were calculated to show the improvement of this study (detail of this table is explained in the text).
[a]The derivation of the values can be found in the text.

of the reasons for this discrepancy between the average elevation values of two data sets may have arisen from the fact that the MGD[3] outline includes the elevation of some nondune and sand aprons areas with the elevation of dune (barchan and barchanoids) areas. An accurate data on the elevation value of dunes is important since it gives qualitative insight into the amount of sediment (dune materials) present in the dune field. MGD[3] has some nondune area included; therefore, MGD[3] is likely to overestimate the amount of sediment in the dune field.

This study calculated the average elevation from the CTX stereo-derived DEM (horizontal resolution ~6 m/pixel), whereas the MGD[3] calculates the average elevation from the MOLA gridded topography raster (horizontal resolution ~463 m/pixel). The differences between elevation data (in terms of spatial resolution) used in this study and the MGD[3] is the reason why there is a slight discrepancy in the elevation measurements. Since the digital elevation data from CTX stereopair were used, which has a higher spatial resolution than the MOLA gridded topography data, the result of this study is likely more reliable. The MGD[3] identified a total area of ~100 km^2 of the dune field at the study area, whereas this study found a total of ~70 km^2 of dune areas. This discrepancy between the estimations is likely due to semiautomated (algorithmically derived) versus manual identification methods as well as this study only calculated dune areas from the individual dunes excluding the outlined surrounding areas whereas inclusion of interdune areas in the MGD[3]. Qualitative validation results show an almost perfect match with the object-based dune distribution as assessed through visual photo inspection from the projected CTX data (Figure 4).

We assessed a statistical analysis of MGD[3] polygon with comparing our output objects-based polygon (hereafter OBIA polygon) to show the improvements in this study. A gross total percent overestimation of the dune field area in the MGD[3] polygon was calculated from the total areal differences between the polygons (30 km^2) divided by the actual area of OBIA polygon (70 km^2). Thus, approximately 42% of the total dune field area was overestimated by MGD[3] polygon (Table 2). Since the MGD[3] polygon did not outline some of the barchan and barchanoidal dunes (e.g., in the south of the dune field; see Figure 1), this study estimated the amount of dune area unmapped by MGD[3]. To calculate this unmapped area, we used ArcGIS's *Analyst Tool* to "erase" the MGD[3] polygon from the OBIA polygon. About 7 km^2 of the dune area (barchan and barchanoids) was unmapped in the MGD[3]. Accordingly, about 63 km^2 of the dune area was correctly outlined by MGD[3] polygon. The percent of unmapped dune area by MGD[3] was calculated from the unmapped dune area (7 km^2) divided by the total area of OBIA polygon (70 km^2), resulting 10% unmapped dune area by MGD[3] (Table 2). That means about 90% of the actual dune field area was outlined by MGD[3]. Within the outline, MGD[3] polygon mapped some nondunes, including sand aprons, area as dune area (see Figure 1), which made an overestimation of barchan and barchanoidal dunes within the outline. Consequently, the OBIA polygon was "erased" from the MGD[3] polygon to calculate the amount of nondune overestimation (inclusion of nondune area to barchan and barchanoidal dune area) within the MGD[3] outline. The nondune overestimation of the dune field was found about 37 km^2 within the MGD[3]. The percent of nondune overestimation was calculated from the area of overestimation (37 km^2) divided by the accurately estimated area by the MGD[3] polygon (63 km^2), resulting in 55% of nondune overestimation within the MGD[3] (Table 2).

We quantitatively assessed the dune classification accuracy. Among a total of 500 points, exactly 291 and 166 points are accurately classified as the corresponding ground truth dune and nondune class, respectively (Table 3). In this study, therefore, a total of 291 + 166 = 457 points was classified correctly among total reference points, which results in an overall accuracy of 91% (Table 4). The kappa value was computed following

Table 3
Details of the Error Matrix of the Classification for the 500 Random Points

Producer accuracy	Number of accurate points	Number of reference points	Percentage (%)
Nondune	166	171	97.08
Dune	291	329	88.45
User accuracy	**Number of accurate points**	**Total number of mapped points**	**Percentage (%)**
Nondune	166	204	81.37
Dune	291	296	98.31

Note. The producer accuracy and user accuracy are listed in the table. The number of accurate points indicates the points that mapped accurately to represent the corresponding reference class points, and the number of a reference point are the points that are known to be correct or ground truth point. The total number of mapped points is the points that were classified, through object-based algorithms, in the respective group (detail of this derivation is given in the text).

the procedure described in the method section. Using the equations (1–3) the kappa value is calculated as approximately 82% in this study (Table 4). A result of kappa values between 0.81 and 1.00 (i.e., 81% to 100%) is considered as an almost perfect agreement (e.g., McHugh, 2012; Viera & Garrett, 2005) between the classified values and ground truth values.

Having provided results showing that the higher classification accuracy (with an overall accuracy of 91%) and validated method (with a kappa value of 0.82), it is argued that the OBIA technique can be applied to the entire Martian surface for an updated dune database. However, the study does point out that the rule set likely will have to be modified for different regions since object-based rule sets are image used and user dependent. A global application of the object-based dune identification depends on the availability of CTX data for creation of the DEM. The output of this study (dune vector file) are available in a public repository for further general use (please see the Data Availability Statement section for details).

The applicability of the algorithm to any kind of Martian dune field depends on the availability of images and DEMs irrespective of dune composition, for instance, gypsum dunes. Even in the case of dunes that are covered by dust, the method can be applied if CTX panchromatic image allows enough spectral contrast and DEM clearly reveals the elevation difference between dunes and nondune features. However, if CTX image products do not allow an appropriate segmentation of dunes objects from image pixels of a scene, we recommend integrating additional image layers from a different sensor into the segmentation algorithm. For instance, the MOC's narrow-angle (MOC-NA; Malin et al., 1992) and/or HiRISE observation layers can be added to the image segmentation routine since both sensors have a higher spatial resolution of typically 1.5 to 12 and 0.25 m/pixel, respectively. Having a comparatively lower spatial resolution, the CRISM (18 to 200 m/pixel) and OMEGA (300 m to 5 km/pixel) sensors images would not be very appropriate for individual dune identification at a local scale. However, the use of an additional image layer(s) in segmentation is a matter of further study where CTX image products are not sufficient for appropriate segmentation.

3.2. Slipface, Wind Movement, and Dune Mobility

The raw slipfaces of the dunes were analyzed to interpret the wind movement inside the crater. We used the slipface information that was prepared by the MGD[3]. A total of 77 raw slipfaces were derived (by the MGD[3])

Table 4
Details of the Error Matrix Result of the Classification for the 500 Random Points

		Reference data		
		Dune	Nondune	Total
Classified data	Dune	291 [P_{11}]	5 [P_{12}]	296 [P_{10}]
	Nondune	38 [P_{21}]	166 [P_{22}]	204 [P_{20}]
	Total	329 [P_{01}]	171 [P_{02}]	500 [P]
Overall accuracy (OA)		0.91% or 91%		
Kappa coefficient (*kappa*)		0.82% or 82%		

Note. The symbols inside the bracket indicate the symbols used for kappa value calculation in the equations (1–3). The overall accuracy and kappa coefficient are listed in the table below.

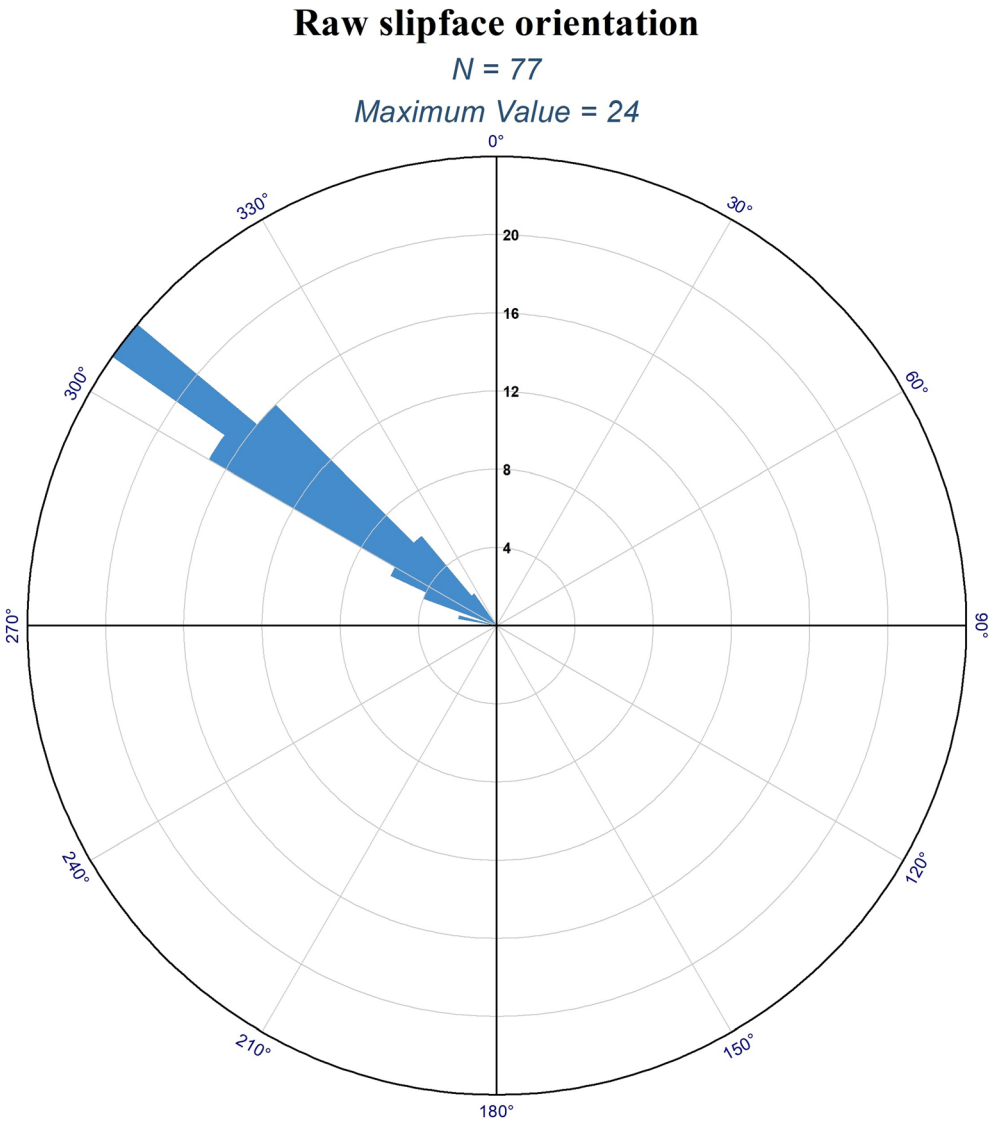

Figure 5. The azimuthal distribution of the raw slipface of the dunes inside the Hargraves crater. A total of 77 raw slipfaces were derived in the crater from the study of Hayward et al. (2007). The calculated raw slipface azimuth of the dunes has a minimum value of 281° to a maximum of 321° with an average slipface value of 306°.

in the study area from the MOC-NA (Malin et al., 1992) observations and THEMIS visible camera images (Hayward et al., 2007). MOC-NA R1102034 and THEMIS-VIS V02781004, V09634019, and V13016004 images were used to measure slipfaces of dunes. One of the rationales of using the existing MGD[3] derived slipface information is that the MOC-NA has a higher spatial resolution (typically 1.5 to 12 m/pixel) than the CTX (~6 m/pixel) image does; therefore, the study did not prepare separate raw slipfaces data for the dunes; rather, it used the existing raw slipface prepared by the MGD[3]. We emphasize that the output of this study in respect of individual dunes' geometric information along with the MGD[3] derived raw slipface would certainly be an important source of the data set for studying local scale dune dynamics and mechanism.

The slipfaces were derived from gross dune morphology at Hargraves crater. The slipfaces indicate the prevailing wind direction of significant dune modification at the last time (Hayward et al., 2007). The work of Hayward et al. (2007) shows that slipface orientations for the dune fields within craters are less correlated with the Martian wind general circulation model (GCM); rather, the dune orientation is predominantly influenced by the effect of the local topography. That is why we also hypothesize that the local topography within the Hargraves crater determines the wind direction, slipface orientation, and eventually the shape of the dunes. The calculated raw slipface azimuth of the dunes has a minimum value of 281° to a maximum of

321° with an average slipface value of 306°. The angular deviation and variance (e.g., Fisher, 1993) were 7.47295° and 0.01701°, respectively. We prepared a rose diagram to describe the raw slipface azimuth of the dunes at Hargraves crater (Figure 5).

The primary wind direction was recorded, in this study, by an estimated average of the individual slipface azimuths discernible from gross dune morphology of different dune types (i.e., barchans and barchanoids) that were shaped by unidirectional winds. Thus, we assert that the prevailing wind movement direction inside the crater is around 306°. Though the temporal movement of the dunes at the crater does not belong to the scope of the present study, we define the dunes in the present study area are active or mobile. The reason for this hypothesis roots into the global latitudinal dune field stability (Fenton et al., 2019; Gullikson et al., 2018). The study of Gullikson et al. (2018) found that the dune fields from the high northern latitude to midsouthern latitude (including the present study area) had no features associated with dune field stability and are thus inferred to be active. We inferred that the dunes at the crater are also active (albeit the annual rate of movement is still unknown) with a wind movement toward west-northwest (306° azimuths).

To confirm the interpretations on dune mobility and modification, the stability index was used for the dunes at Hargraves crater. We did not find any of noneolian features; however, there is a thin sand apron present on the western part of the dune field (Figure 4). Based on visual inspection, it is posited that the dune field has a stability index of 2; the dunes are partially surrounded by crisp-edged sandy aprons that do not completely merge with those of neighboring dunes. The study of Fenton and Hayward (2010) has identified, based on the observations of stability parameters and morphologies, that the dunes at southern high latitudes are modified by the surface ice or other volatiles. Having the absence of these stability indicators and morphologies, we suggest that unlike the dunes at southern high latitudes, the dunes at Hargraves crater are not modified or influenced by the subsurface water ice or other volatiles.

4. Conclusion

The delineation of dune fields in MGD^3 was prepared manually through visual photointerpretation from the THEMIS imagery at 100 m/pixel spatial resolution, including the digitized dune parameters and mapped dune slipface orientations. Though the MGD^3 outlines dunes fields, it does not delineate individual dunes within the dune fields. Moreover, the manual digitization of individual dune parameters from the lower resolution THEMIS images is a tedious and time-consuming task. Thus, a semiautomated method from higher-resolution images, for example, CTX at ~6 m/pixel, can be used more efficiently to extract significant morphological information about the Martian dune fields. This study employed a semiautomated OBIA technique to extract dunes at Hargraves crater as a test case of OBIA application. The validated and relatively accurate results indicate the applicability of the OBIA method for dune mapping for the entire surface of Mars. The wind movement was analyzed inside the crater from the dune slipface orientation, which indicates the prevailing wind direction inside the crater toward the west-northwest. The dune field was identified as having active dunes with a stability index of 2.

Appendix A: CTX and HiRISE Observations

We used observations from CTX and HiRISE sensors data. CTX products from Radiometric Data Record (RDR) and Stereopair images were used in the object-based image analysis algorithm. CTX raw images are converted into reflectance (irradiance/solar flux or I/F) to produce RDR data. HiRISE Extended Science Phase (ESP) data products were used as the supplementary imagery in this study. A detailed list of the observations used, that is, image type and IDs, is given in Table A1. The images were downloaded from the PDS Geosciences Node.

Table A1
List of Images Used in This Study

Sensor	Image type	Image ID
CTX	Stereopair/RDR	D14_032860_2009, D15_033071_2009
HiRISE	ESP	ESP_028390_2010, ESP_030091_2010, ESP_030302_2010, ESP_051097_2010

Data Availability Statement

The data for finally extracted dunes in an ArcGIS vector file (.shp format) are available from a public repository. The data have been archived in the Mendeley Dataset repository (https://data.mendeley.com/datasets/bfnxzwhd4r/3). Please cite the data as Emran, A., Marzen, L., King, D., 2019. Dune data set for Hargraves crater, Mars (https://doi.org/10.17632/bfnxzwhd4r.3).

Acknowledgments

The authors would like to thank the team members of the 2001 Mars Odyssey and Mars Reconnaissance Orbiter (MRO) spacecraft missions for targeting, collecting, and archiving THEMIS, CTX, and HiRISE data sets. JMARS, ISIS3, Ames Stereo Pipelines (ASP), eCognition, and ArcGIS software were used for data processing and analysis. The author would also like to thank Jennifer Buz and two other anonymous referees for their useful comments.

References

Baatz, M., Hoffmann, C., & Willhauck, G. (2008). Progressing from object-based to object-oriented image analysis. In *Object-based image analysis, Lecture Notes in Geoinformation and Cartography* (pp. 29–42). Berlin, Heidelberg: Springer.

Baatz, M., & Schäpe, M. (2000). Multiresolution segmentation—An optimization approach for high quality multi-scale image segmentation. In J. Strobl, T. Blaschke, & G. Griesebner (Eds.), *Angewandte geographische informations-Verarbeitung XII* (pp. 12–23). Karlsruhe: Wichmann Verlag.

Bandeira, L., Marques, J. S., Saraiva, J., & Pina, P. (2010). Automated detection of sand dunes on Mars. In *Image analysis and recognition, Lecture Notes in Computer Science* (pp. 306–315). Berlin, Heidelberg: Springer.

Bandeira, L., Marques, J. S., Saraiva, J., & Pina, P. (2011). Automated detection of Martian dune fields. *IEEE Geoscience and Remote Sensing Letters*, *8*(4), 626–630. https://doi.org/10.1109/LGRS.2010.2098390

Banks, M. E., Fenton, L. K., Bridges, N. T., Geissler, P. E., Chojnacki, M., Runyon, K. D., et al. (2018). Patterns in mobility and modification of middle- and high-latitude southern hemisphere dunes on Mars. *Journal of Geophysical Research: Planets*, *123*, 3205–3219. https://doi.org/10.1029/2018JE005747

Benz, U. C., Hofmann, P., Willhauck, G., Lingenfelder, I., & Heynen, M. (2004). Multi-resolution, object-oriented fuzzy analysis of remote sensing data for GIS-ready information. *ISPRS Journal of Photogrammetry and Remote Sensing, Integration of Geodata and Imagery for Automated Refinement and Update of Spatial Databases*, *58*(3-4), 239–258. https://doi.org/10.1016/j.isprsjprs.2003.10.002

Beyer, R. A., Alexandrov, O., & Moratto, Z. M. (2014). *Aligning terrain model and laser altimeter point clouds with the Ames Stereo Pipeline* (p. 2902). Presented at the Lunar and Planetary Science Conference.

Blaschke, T. (2010). Object based image analysis for remote sensing. *ISPRS Journal of Photogrammetry and Remote Sensing*, *65*(1), 2–16. https://doi.org/10.1016/j.isprsjprs.2009.06.004

Blaschke, T., Hay, G. J., Kelly, M., Lang, S., Hofmann, P., Addink, E., et al. (2014). Geographic object-based image analysis—Towards a new paradigm. *ISPRS Journal of Photogrammetry and Remote Sensing*, *87*(100), 180–191. https://doi.org/10.1016/j.isprsjprs.2013.09.014

Blaschke, T., & Strobl, J. (2002). What's wrong with pixels? Some recent developments interfacing remote sensing and GIS. *GIS–Zeitschrift für Geoinformationssysteme*, *14*(6), 12–17.

Broxton, M. J., & Edwards, L. J. (2008). *The Ames Stereo Pipeline: Automated 3D surface reconstruction from orbital imagery* (p. 2419). Presented at the Lunar and Planetary Science Conference.

Burnett, C., & Blaschke, T. (2003). A multi-scale segmentation/object relationship modelling methodology for landscape analysis. *Ecological Modelling, Landscape Theory and Landscape Modelling*, *168*, 233–249. https://doi.org/10.1016/S0304-3800(03)00139-X

Burrough, P. A., McDonnell, R. A., & Lloyd, C. D. (2015). *Principles of geographical information systems* (3rd ed.). Oxford; New York: Oxford University Press.

Castilla, G., & Hay, G. J. (2008). Image objects and geographic objects. In *Object-based image analysis, Lecture Notes in Geoinformation and Cartography* (pp. 91–110). Berlin, Heidelberg: Springer.

Christensen, P. R., Jakosky, B. M., Kieffer, H. H., Malin, M. C., McSween, H. Y., Nealson, K., et al. (2004). The Thermal Emission Imaging System (THEMIS) for the Mars 2001 Odyssey mission. *Space Science Reviews*, *110*(1/2), 85–130. https://doi.org/10.1023/B:SPAC.0000021008.16305.94

Congalton, R. G. (1991). A review of assessing the accuracy of classifications of remotely sensed data. *Remote Sensing of Environment*, *37*(1), 35–46. https://doi.org/10.1016/0034-4257(91)90048-B

Congalton, R. G., & Green, K. (2008). *Assessing the accuracy of remotely sensed data: Principles and practices* (2nd ed.). Boca Raton: CRC Press.

Darwish, A., Leukert, K., & Reinhardt, W. (2003). *Image segmentation for the purpose of object-based classification* (pp. 2039–2041). Paper presented at 2003 IEEE International Geoscience and Remote Sensing Symposium (IGARSS). https://doi.org/10.1109/IGARSS.2003.1294332

Delamere, W. A., Tornabene, L. L., McEwen, A. S., Becker, K., Bergstrom, J. W., Bridges, N. T., et al. (2010). Color imaging of Mars by the High Resolution Imaging Science Experiment (HiRISE). *Icarus, MRO/HiRISE Studies of Mars*, *205*(1), 38–52. https://doi.org/10.1016/j.icarus.2009.03.012

du Pont, S. C., Narteau, C., & Gao, X. (2014). Two modes for dune orientation. *Geology*, *42*(9), 743–746. https://doi.org/10.1130/G35657.1

Duro, D. C., Franklin, S. E., & Dubé, M. G. (2012). A comparison of pixel-based and object-based image analysis with selected machine learning algorithms for the classification of agricultural landscapes using SPOT-5 HRG imagery. *Remote Sensing of Environment*, *118*, 259–272. https://doi.org/10.1016/j.rse.2011.11.020

Edgett, K. S., & Christensen, P. R. (1991). The particle size of Martian aeolian dunes. *Journal of Geophysical Research*, *96*(E5), 22,765–22,776. https://doi.org/10.1029/91JE02412

Edgett, K. S., & Malin, M. C. (2000). New views of Mars eolian activity, materials, and surface properties: Three vignettes from the Mars Global Surveyor Mars Orbiter Camera. *Journal of Geophysical Research, 105*(E1), 1623–1650. https://doi.org/10.1029/1999JE001152

Elbelrhiti, H., Andreotti, B., & Claudin, P. (2008). Barchan dune corridors: Field characterization and investigation of control parameters. *Journal of Geophysical Research*, *113*, F02S15. https://doi.org/10.1029/2007JF000767

Emran, A., Marzen, L. J., & King, D. T. (2019). *Automated object-based identification of dunes at Hargraves crater, Mars* (p. 1157). Presented at the Lunar and Planetary Science Conference.

Fenton, L. K., Gullikson, A. L., Hayward, R. K., Charles, H., & Titus, T. N. (2019). *The Mars Global Digital Dune Database (MGD^3): Composition and stability* (p. 1115). Presented at the Lunar and Planetary Science Conference.

Fenton, L. K., & Hayward, R. K. (2010). Southern high latitude dune fields on Mars: Morphology, aeolian inactivity, and climate change. *Geomorphology, Planetary Dune Systems*, *121*(1–2), 98–121. https://doi.org/10.1016/j.geomorph.2009.11.006

Fenton, L. K., Michaels, T. I., & Beyer, R. A. (2014). Inverse maximum gross bedform-normal transport 1: How to determine a dune-constructing wind regime using only imagery. *Icarus, Third Planetary Dunes Systems*, *230*, 5–14. https://doi.org/10.1016/j.icarus.2013.04.001

Fenton, L. K., Michaels, T. I., Chojnacki, M., & Beyer, R. A. (2014). Inverse maximum gross bedform-normal transport 2: Application to a dune field in Ganges Chasma, Mars and comparison with HiRISE repeat imagery and MRAMS. *Icarus, Third Planetary Dunes Systems*, *230*, 47–63. https://doi.org/10.1016/j.icarus.2013.07.009

Fenton, L. K., Toigo, A. D., & Richardson, M. I. (2005). Aeolian processes in Proctor Crater on Mars: Mesoscale modeling of dune-forming winds. *Journal of Geophysical Research*, *110*, E06005. https://doi.org/10.1029/2004JE002309

Fisher, N. I. (1993). *Statistical analysis of circular data* [WWW document]. Cambridge Core. https://doi.org/10.1017/CBO9780511564345

Fisher, P. (1997). The pixel: A snare and a delusion. *International Journal of Remote Sensing*, *18*(3), 679–685. https://doi.org/10.1080/014311697219015

Foody, G. M. (2002). Status of land cover classification accuracy assessment. *Remote Sensing of Environment*, *80*(1), 185–201. https://doi.org/10.1016/S0034-4257(01)00295-4

Gardin, E., Allemand, P., Quantin, C., Silvestro, S., & Delacourt, C. (2012). Dune fields on Mars: Recorders of a climate change? *Planetary and Space Science, Titan Through Time: A Workshop on Titan's Formation, Evolution and Fate*, *60*(1), 314–321. https://doi.org/10.1016/j.pss.2011.10.004

Goudge, T. A., Milliken, R. E., Head, J. W., Mustard, J. F., & Fassett, C. I. (2017). Sedimentological evidence for a deltaic origin of the western fan deposit in Jezero crater, Mars and implications for future exploration. *Earth and Planetary Science Letters*, *458*, 357–365. https://doi.org/10.1016/j.epsl.2016.10.056

Goudge, T. A., Mustard, J. F., Head, J. W., Fassett, C. I., & Wiseman, S. M. (2015). Assessing the mineralogy of the watershed and fan deposits of the Jezero crater paleolake system, Mars. *Journal of Geophysical Research: Planets*, *120*, 775–808. https://doi.org/10.1002/2014JE004782

Greeley, R., Kuzmin, R. O., & Haberle, R. M. (2001). Aeolian processes and their effects on understanding the chronology of Mars. *Space Science Reviews*, *96*(1/4), 393–404. https://doi.org/10.1023/A:1011917910624

Greeley, R., & Thompson, S. D. (2003). Mars: Aeolian features and wind predictions at the Terra Meridiani and Isidis Planitia potential Mars Exploration Rover landing sites. *Journal of Geophysical Research*, *108*(E12), 8093. https://doi.org/10.1029/2003JE002110

Gullikson, A. L., Hayward, R. K., Titus, T. N., Charles, H., Fenton, L. K., Hoover, R. H., & Putzig, N. E. (2018). Mars global digital dune database (MGD3)—Composition, stability, and thermal inertia (USGS numbered series no. 2018–1164), Open-File Report. U.S. Geological Survey, Reston, VA.

Hay, G. J., Blaschke, T., Marceau, D. J., & Bouchard, A. (2003). A comparison of three image-object methods for the multiscale analysis of landscape structure. *ISPRS Journal of Photogrammetry and Remote Sensing, Challenges in Geospatial Analysis and Visualization*, *57*, 327–345. https://doi.org/10.1016/S0924-2716(02)00162-4

Hay, G. J., & Castilla, G. (2008). Geographic Object-Based Image Analysis (GEOBIA): A new name for a new discipline. In *Object-based image analysis, Lecture Notes in Geoinformation and Cartography* (pp. 75–89). Berlin, Heidelberg: Springer.

Hayward, R. K., Fenton, L., & Titus, T. N. (2014). Mars Global Digital Dune Database (MGD3): Global dune distribution and wind pattern observations. *Icarus*, *230*, 38–46. https://doi.org/10.1016/j.icarus.2013.04.011

Hayward, R. K., Mullins, K. F., Fenton, L. K., Hare, T. M., Titus, T. N., Bourke, M. C., et al. (2007). Mars global digital dune database and initial science results. *Journal of Geophysical Research*, *112*, E11007. https://doi.org/10.1029/2007JE002943

Hayward, R. K., Titus, T. N., Michaels, T. I., Fenton, L. K., Colaprete, A., & Christensen, P. R. (2009). Aeolian dunes as ground truth for atmospheric modeling on Mars. *Journal of Geophysical Research*, *114*, E11012. https://doi.org/10.1029/2009JE003428

Hugenholtz, C. H., Levin, N., Barchyn, T. E., & Baddock, M. C. (2012). Remote sensing and spatial analysis of aeolian sand dunes: A review and outlook. *Earth-Science Reviews*, *111*(3-4), 319–334. https://doi.org/10.1016/j.earscirev.2011.11.006

Ivanov, M. A., Hiesinger, H., Erkeling, G., Hielscher, F. J., & Reiss, D. (2012). Major episodes of geologic history of Isidis Planitia on Mars. *Icarus*, *218*(1), 24–46. https://doi.org/10.1016/j.icarus.2011.11.029

Jones, T., Marzen, L., Mitra, C., & Barbour, M. (2019). Identification and classification of geographically isolated wetlands in North Alabama using geographic object based image analysis (GeOBIA). *Geocarto International*, *34*(7), 769–784. https://doi.org/10.1080/10106049.2018.1438527

Kim, M., Madden, M., & Warner, T. (2008). Estimation of optimal image object size for the segmentation of forest stands with multispectral IKONOS imagery. In T. Blaschke, S. Lang, & G. J. Hay (Eds.), *Object-based image analysis: Spatial concepts for knowledge-driven remote sensing applications, lecture notes in geoinformation and cartography* (pp. 291–307). Berlin, Heidelberg: Springer.

Kim, M., Warner, T. A., Madden, M., & Atkinson, D. S. (2011). Multi-scale GEOBIA with very high spatial resolution digital aerial imagery: Scale, texture and image objects. *International Journal of Remote Sensing*, *32*, 2825–2850. https://doi.org/10.1080/01431161003745608

Liu, Y., Bian, L., Meng, Y., Wang, H., Zhang, S., Yang, Y., et al. (2012). Discrepancy measures for selecting optimal combination of parameter values in object-based image analysis. *ISPRS Journal of Photogrammetry and Remote Sensing*, *68*, 144–156. https://doi.org/10.1016/j.isprsjprs.2012.01.007

Malin, M. C., Bell, J. F., Cantor, B. A., Caplinger, M. A., Calvin, W. M., Clancy, R. T., et al. (2007). Context Camera investigation on board the Mars Reconnaissance Orbiter. *Journal of Geophysical Research*, *112*, E05S04. https://doi.org/10.1029/2006JE002808

Malin, M. C., Danielson, G. E., Ingersoll, A. P., Masursky, H., Veverka, J., Ravine, M. A., & Soulanille, T. A. (1992). Mars observer camera. *Journal of Geophysical Research*, *97*(E5), 7699–7718. https://doi.org/10.1029/92JE00340

Marpu, P. R., Neubert, M., Herold, H., & Niemeyer, I. (2010). Enhanced evaluation of image segmentation results. *Journal of Spatial Science*, *55*(1), 55–68. https://doi.org/10.1080/14498596.2010.487850

McEwen, A. S., Eliason, E. M., Bergstrom, J. W., Bridges, N. T., Hansen, C. J., Delamere, W. A., et al. (2007). Mars reconnaissance orbiter's High Resolution Imaging Science Experiment (HiRISE). *Journal of Geophysical Research*, *112*, E05S02. https://doi.org/10.1029/2005JE002605

McHugh, M. L. (2012). Interrater reliability: The kappa statistic. *Biochem Med (Zagreb)*, *22*, 276–282.

McKee, E. D., United States, National Aeronautics and Space Administration, & U.S. Geological Survey (1979). *A study of global sand seas*. Washington: U.S. Government Printing Office.

Moratto, Z. M., Broxton, M. J., Beyer, R. A., Lundy, M., & Husmann, K. (2010). *Ames Stereo Pipeline, NASA's open source automated stereogrammetry software* (p. 2364). Presented at the Lunar and Planetary Science Conference.

Myint, S. W., Gober, P., Brazel, A., Grossman-Clarke, S., & Weng, Q. (2011). Per-pixel vs. object-based classification of urban land cover extraction using high spatial resolution imagery. *Remote Sensing of Environment*, *115*(5), 1145–1161. https://doi.org/10.1016/j.rse.2010.12.017

Quantin-Nataf, C., Lozac'h, L., Thollot, P., Loizeau, D., Bultel, B., Fernando, J., et al. (2018). MarsSI: Martian surface data processing information system. *Planetary and Space Science, Enabling Open and Interoperable Access to Planetary Science and Heliophysics Databases and Tools*, *150*, 157–170. https://doi.org/10.1016/j.pss.2017.09.014

Riley, S. J., De Gloria, S. D., & Elliot, R. (1999). A terrain ruggedness that quantifies topographic heterogeneity. *Intermountain Journal of Science*, *5*(1–4), 23–27.

Sagan, C., Veverka, J., Fox, P., Dubisch, R., Lederberg, J., Levinthal, E., et al. (1972). Variable features on Mars: Preliminary mariner 9 television results. *Icarus*, *17*(2), 346–372. https://doi.org/10.1016/0019-1035(72)90005-X

Sefton-Nash, E., Teanby, N. A., Newman, C., Clancy, R. A., & Richardson, M. I. (2014). Constraints on Mars' recent equatorial wind regimes from layered deposits and comparison with general circulation model results. *Icarus, Third Planetary Dunes Systems*, *230*, 81–95. https://doi.org/10.1016/j.icarus.2013.11.014

Sholes, S. F., Chevrier, V. F., & Tullis, J. A. (2013). *Object based image analysis for remote sensing of planetary surfaces*. Paper presented at 44th Lunar and Planetary Science Conference, Houston, TX.

Silvestro, S., Di Achille, G., & Ori, G. G. (2010). Dune morphology, sand transport pathways and possible source areas in east Thaumasia Region (Mars). *Geomorphology, Planetary Dune Systems*, *121*(1–2), 84–97. https://doi.org/10.1016/j.geomorph.2009.07.019

Silvestro, S., Vaz, D. A., Ewing, R. C., Rossi, A. P., Fenton, L. K., Michaels, T. I., et al. (2013). Pervasive aeolian activity along rover Curiosity's traverse in Gale Crater, Mars. *Geology*, *41*(4), 483–486. https://doi.org/10.1130/G34162.1

Smith, A. (2010). Image segmentation scale parameter optimization and land cover classification using the Random Forest algorithm. *Journal of Spatial Science*, *55*(1), 69–79. https://doi.org/10.1080/14498596.2010.487851

Smith, D. E., Zuber, M. T., Frey, H. V., Garvin, J. B., Head, J. W., Muhleman, D. O., et al. (2001). Mars Orbiter Laser Altimeter: Experiment summary after the first year of global mapping of Mars. *Journal of Geophysical Research*, *106*(E10), 23,689–23,722. https://doi.org/10.1029/2000JE001364

Strahler, A. H., Woodcock, C. E., & Smith, J. A. (1986). On the nature of models in remote sensing. *Remote Sensing of Environment*, *20*(2), 121–139. https://doi.org/10.1016/0034-4257(86)90018-0

Tian, J., & Chen, D.-M. (2007). Optimization in multi-scale segmentation of high-resolution satellite images for artificial feature recognition. *International Journal of Remote Sensing*, *28*(20), 4625–4644. https://doi.org/10.1080/01431160701241746

Tong, H., Maxwell, T., Zhang, Y., & Dey, V. (2012). *A supervised and fuzzy-based approach to determine optimal multi-resolution image segmentation parameters* [WWW Document]. https://doi.org/10.14358/PERS.78.10.1029

Tzotsos, A., & Argialas, D. (2008). Support vector machine classification for object-based image analysis. In *Object-based image analysis, Lecture Notes in Geoinformation and Cartography* (pp. 663–677). Berlin, Heidelberg: Springer.

Vaz, D. A., Sarmento, P. T. K., Barata, M. T., Fenton, L. K., & Michaels, T. I. (2015). Object-based Dune Analysis: Automated dune mapping and pattern characterization for Ganges Chasma and Gale crater, Mars. *Geomorphology*, *250*, 128–139. https://doi.org/10.1016/j.geomorph.2015.08.021

Vaz, D. A., & Silvestro, S. (2014). Mapping and characterization of small-scale aeolian structures on Mars: An example from the MSL landing site in Gale Crater. *Icarus, Third Planetary Dunes Systems*, *230*, 151–161. https://doi.org/10.1016/j.icarus.2013.08.007

Viera, A. J., & Garrett, J. M. (2005). Understanding interobserver agreement: The kappa statistic. *Family Medicine*, *37*(5), 360–363.

Ward, A. W., Doyle, K. B., Helm, P. J., Weisman, M. K., & Witbeck, N. E. (1985). Global map of eolian features on Mars. *Journal of Geophysical Research*, *90*, 19.

Wilson, S. A., & Zimbelman, J. R. (2004). Latitude-dependent nature and physical characteristics of transverse aeolian ridges on Mars. *Journal of Geophysical Research*, *109*, E10. https://doi.org/10.1029/2004JE002247

Witharana, C., & Civco, D. L. (2014). Optimizing multi-resolution segmentation scale using empirical methods: Exploring the sensitivity of the supervised discrepancy measure Euclidean distance 2 (ED2). *ISPRS Journal of Photogrammetry and Remote Sensing*, *87*, 108–121. https://doi.org/10.1016/j.isprsjprs.2013.11.006

Zurek, R. W., & Smrekar, S. E. (2007). An overview of the Mars Reconnaissance Orbiter (MRO) science mission. *Journal of Geophysical Research*, *112*, E05S01. https://doi.org/10.1029/2006JE002701